



저작자표시-비영리-변경금지 2.0 대한민국

이용자는 아래의 조건을 따르는 경우에 한하여 자유롭게

- 이 저작물을 복제, 배포, 전송, 전시, 공연 및 방송할 수 있습니다.

다음과 같은 조건을 따라야 합니다:



저작자표시. 귀하는 원저작자를 표시하여야 합니다.



비영리. 귀하는 이 저작물을 영리 목적으로 이용할 수 없습니다.



변경금지. 귀하는 이 저작물을 개작, 변형 또는 가공할 수 없습니다.

- 귀하는, 이 저작물의 재이용이나 배포의 경우, 이 저작물에 적용된 이용허락조건을 명확하게 나타내어야 합니다.
- 저작권자로부터 별도의 허가를 받으면 이러한 조건들은 적용되지 않습니다.

저작권법에 따른 이용자의 권리는 위의 내용에 의하여 영향을 받지 않습니다.

이것은 [이용허락규약\(Legal Code\)](#)을 이해하기 쉽게 요약한 것입니다.

[Disclaimer](#)

공학석사 학위논문

Chiral Surface-Driven Optical Image Selection by Polarization in Liquid Crystal Devices

액정 장치에서의 편광을 통한 카이랄 표면 구동
이미지 선택

2018 년 2 월

서울대학교 대학원

공과대학 전기·정보공학부

이 상 현

Chiral Surface-Driven Optical Image Selection by Polarization in Liquid Crystal Devices

액정 장치에서의 편광을 통한 카이랄 표면 구동
이미지 선택

지도 교수 이 신 두
이 논문을 공학석사 학위논문으로 제출함
2018 년 2 월
서울대학교 대학원
공과대학 전기·정보공학부
이 상 현

이상현의 공학석사 학위논문을 인준함
2017 년 12 월

위 원 장 이 병 호 (인)

부위원장 이 신 두 (인)

위 원 정 윤 찬 (인)

Abstract

Recently, many approaches have been developed to construct different images depending on the polarization state of light. Constructing different images depending on the polarization state of light has various applications such as optical image storage systems, stereoscopic three-dimensional (3D) displays, and anti-counterfeiting. In previous studies, optical image selection through linear polarization state of light has extensively studied due to the simple polarization state generation through polarizers and through intuitive structures of the image generating systems. However, image selection through linear polarization has a severe disadvantage that the alignment of the polarizer and the polarization state of the image should be aligned perfectly. For example, 3D displays using linear polarization cannot show the 3D images when the viewer does not see the

display in a straight way. To be specific, if the viewer sees the display in a lying position, the 3D images are not constructed due to the misalignment of the polarizers on the viewer's eyes and the polarization state from the 3D display. To overcome such drawbacks, image selection through circularly polarized light has been demonstrated since circular polarization does not depend on the alignment direction. To retrieve circular polarization, chiral structures or phase retarders have been used. However, previous studies were limited in their polarization switching capability, which could enhance the quality and the applicable range of these systems. Also, simple fabrication of such circular polarization generating structures are required for practical applications.

This thesis demonstrates chiral surface-driven images in liquid crystal devices with polarization switching capability that can be selected according to the polarization state of the viewing polarizer. The patterned surface chiral layer reflects a circularly polarized light with a certain color. The homogeneous LC layer placed on the patterned surface chiral layer acts

as a tunable wave retarder that modifies the polarization state of the reflected light from the surface chiral layer. Depending on the applied voltage across the LC layer, either right-handed or left-handed circular polarized images are produced so that selective reading of recorded images can be achieved with a polarization detector. Our polarization switchable image selection allows simple fabrication, higher quality, and diverse usage for visual applications including displays and image storage systems.

Keyword: Optical image selection, Chiral reactive mesogen, Circular polarization, Liquid crystals

Student Number: 2016-20949

Table of Contents

Abstract	i
Table of Contents	iv
List of Figures	vi
List of Tables	ix
Chapter 1 Introduction.....	1
1.1 Optical Image Selection According to the Polarization State	1
1.2 Surface Chiral Images with Polarization Switching Capability by Tunable Phase Retarder	3
1.3 Outline of Thesis	7
Chapter 2 Theoretical Background	9
2.1 Cholesteric Liquid Crystals and Chiral Reactive Mesogen	9
2.2 Stokes Parameters and Mueller Matrix	13
2.3 Nematic Liquid Crystals as a Tunable Wave Retarder	17
2.4 Berreman 4x4 Propagation Matrix Method	19
Chapter 3 Experiments	33
3.1 Patterned Indium-Tin-Oxide (ITO) Substrate	33
3.2 Preparation of Surface Chiral Images.....	35

3.3 Fabrication of Polarization Switchable LC Cell	37
Chapter 4 Results and Discussion.....	40
4.1 Polarization Dependent Reflecting Properties of the Chiral Surface-Driven Optical Images in LC Devices	40
4.2 Electro-optical Characteristics of the Chiral Surface-Driven Optical Images in LC Devices	44
4.3 Surface Chiral Images with Different Helical Pitch in Chiral RM Layer	47
4.4 Switching Capability with Pixelated Surface Chiral Images	49
4.5 Optical Image Selection by Polarization	52
Chapter 5 Conclusion.....	55
Bibliography	57
초록	62

List of Figures

Figure 1.1 Optical image selection through linear polarization of the light [10].	2
Figure 1.2 Schematic diagram showing our concept of the chiral surface-driven optical image selection by polarization in LC devices: (a) the voltage applied image selected by the RHC filter and (b) the image under no applied voltage selected by the LHC filter.....	5
Figure 1.3 Schematic diagrams of the operation principles of the chiral surface-driven optical image selection by polarization: (a) under no applied voltage and (b) in the presence of the applied voltage.....	6
Figure 2.1 Schematic illustration of the CLC.	11
Figure 2.2 The schematic diagram of (a) the RMs and (b) the liquid crystalline polymer formed through the polymerization of RMs. ..	12
Figure 2.3 Experimental (dashed) and simulation (line) reflectance spectra of (a) B1, (b) G1, and (c) R1.	25
Figure 2.4 Experimental (dashed) and simulation (line) reflectance spectra of (a) B2, (b) G2, and (c) R2.	27
Figure 2.5 Schematic diagram of the stacked surface chiral structure. Surface chiral layer #1 is B1, G1, or R1, and surface chiral layer #2 is B2, G2, or R2, respectively.....	29
Figure 2.6 Experimental (dashed) and simulation (line) reflectance spectra of	

stacked surface chiral structures consisted of (a) B1&B2, (b) G1&G2, and (c) R1&R2. 30

Figure 3.1 Fabrication process of isolating ITO pixels: (a) Plane ITO substrate. (b) PR spin-coating on the ITO substrate for etching mask. (c) UV exposure for patterning PR. (d) Developing PR. (e) Wet etching ITO. (f) Removing the PR..... 33

Figure 3.2 Fabrication process of the patterned surface chiral images: (a) Preparation of surface chiral layer through spin-coating RMS mixture on a patterned ITO glass with alignment layer. (b) Patterned photo-polymerization through UV exposure. (c) Washout process of unpolymerized RMS..... 35

Figure 3.3 Fabrication process of the LC cell: (a) Assembling a cell with anti-parallel rubbing direction of the bottom and the top substrate. (b) Injection of LC in the cell through capillary action. 37

Figure 4.1 Theoretical and experimental reflection spectra according to the applied voltage and the filter type. Reflection spectra with (a) no filter, (b) RHC filter, and (c) LHC filter. The upper-right insets in all figures show the microscopic images of our device depending on the applied voltage. Scale bars represent 500 μm 43

Figure 4.2 The numerical and experimental electro-optical properties of our device. (a) The Stokes parameter, S_3 as a function of applied voltage. (b) The reflectance with simulation RHC filter (red line), experiment RHC filter (red dot), simulation LHC filter (yellow line),

and experiment LHC filter (yellow dot) as a function of voltage... 46

Figure 4.3 The microscopic images with different pitch length in the surface chiral pixel. The pixels are prepared with (a)-(c) green coloration and (d)-(f) blue coloration. The voltage was applied identically on the left pixels. Reflection through no filter with (a) green and (d) blue coloration, RHC filter with (b) green and (e) blue coloration, and LHC filter with (c) green and (f) blue coloration are shown. Scale bar are 500 μm 48

Figure 4.4 The microscopic images of the switching ability through the applied voltage on each pixels viewed through the (a)-(c) RHC filter and the (d)-(f) LHC filter. The voltage maps on the pixels are shown on the top of the images. Scale bars are 500 μm 51

Figure 4.5 Image selection with orthogonal circular polarizers. (a) The surface chiral layer was patterned with the word ‘SNU’ and ‘MIPD’. The voltage was applied on the upper side, where the word ‘SNU’ is inscribed. Only the word (b) ‘SNU’ was retrieved through the RHC filter, and the word (c) ‘MIPD’ was retrieved through the LHC filter. Scale bars are 500 μm 53

List of Tables

Table 2.1 Stokes vector for various polarization states.....	15
Table 2.2 Mueller matrices for common optical elements.....	16
Table 2.3 Simulation pitch lengths for each surface chiral layers.....	23
Table 2.4 Peak wavelengths for each surface chiral layers.....	24

Chapter 1 Introduction

1.1 Optical Image Selection According to the Polarization State

In recent years, optical image selection have attracted much attention for the variety of optical applications such as optical data storage devices [1-5], color filters [6-11], three-dimensional (3D) displays [12-17], and anti-counterfeiting [18-21]. Image selection has been done depending on various conditions, for example, the polarization state of the light [1, 4, 13], the viewing position [8, 14], the wavelength of the light [5, 22], and the appliance of external stimuli [20]. Among these conditions, retrieving different images depending on the polarization state have been extensively studied due to their intuitive structure of the image system and the simple retrieval of images through different polarizers. For instance, as shown in Fig. 1.1, polarization

dependent color filters utilized asymmetric plasmonic nanostructure pixels to represent different colors on different polarization[7, 9, 11], which eventually construct different images retrieved by orthogonal linear polarizers.

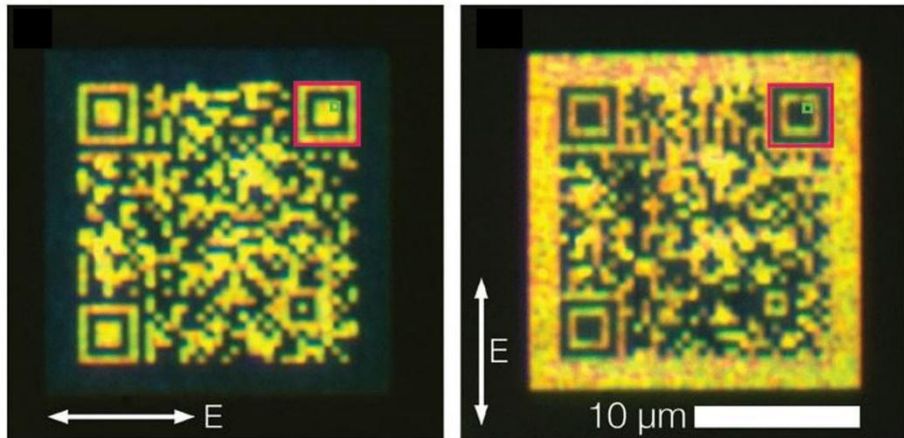


Figure 1.1 Optical image selection through linear polarization of the light [10].

These applications, however, usually employ linearly polarized lights, which gives limitation that the polarized direction of the light and the polarizer should be exactly parallel to obtain the designed image with no error. To overcome such difficulty, circularly polarized lights with different

handedness have been employed since circular polarizers have no absolute axis [15, 16]. However, these systems usually lack their switching ability in the polarization state of light from right-handed circular polarization (RHC) to left-handed circular polarization (LHC), or vice versa. Moreover, surfaces generating circularly polarized lights should be obtained by simple fabrication process for practical applications. As a result, it is strongly required to achieve image selection through a simple fabricated, polarization switchable, circularly polarized light generating system.

1.2 Surface Chiral Images with Polarization Switching Capability by Tunable Phase Retarder

Throughout this thesis, we present a novel concept of a chiral surface-driven images in liquid crystal (LC) devices having polarization switching capability for image selection. The schematic diagram of our concept of LC-based surface chiral images is depicted in Fig. 1.2. A patterned

right-handed surface chiral layer, which reflects right-handed circularly polarized light that matches with the photonic stop band, is placed on the bottom of our device. The LC layer acts as an electrically tunable wave-retarder which changes the polarization state of the reflected light from the surface chiral layer. LC is a perfect material for such system due to the simple fabrication, the high electro-optical anisotropy, and the driving at low voltage. With a RHC filter, as shown in Fig. 1.2(a), only the image from ‘on-state’ is visible, the alphabet ‘A’, while the ‘off-state’ image is invisible. In contrast, with a LHC filter, image seen from the RHC filter is invisible, and only the image from ‘off-state’, alphabet ‘B’, is visible, as shown in Fig. 1.2(b). This means that within the same filter, the image can be selected according to the voltage state, and the same voltage state image can be selected depending on the filter type.

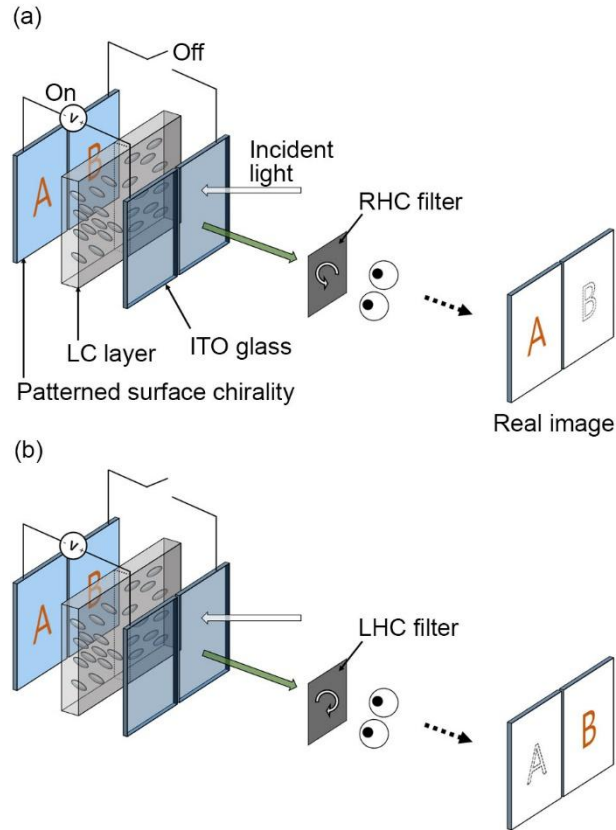


Figure 1.2 Schematic diagram showing our concept of the chiral surface-driven optical image selection by polarization in LC devices:

(a) the voltage applied image selected by the RHC filter and (b) the image under no applied voltage selected by the LHC filter.

The operating principle is depicted in Fig. 1.3. The thickness of the LC layer is designed so that the homogeneously aligned LC layer becomes a

half-wave retarder at the wavelength of the reflected light from the surface chiral layer. In initial state, as shown in Fig. 1.3(a), the RHC light from the surface chiral layer switches its polarization state to LHC so that the LHC image is produced from the off-state area. With an applied voltage (on-state), as shown in Fig. 1.3(b), the LC is aligned perpendicularly to the substrate. In this state, the reflected image from the surface chiral layer does not change its polarization, eventually producing a RHC image.

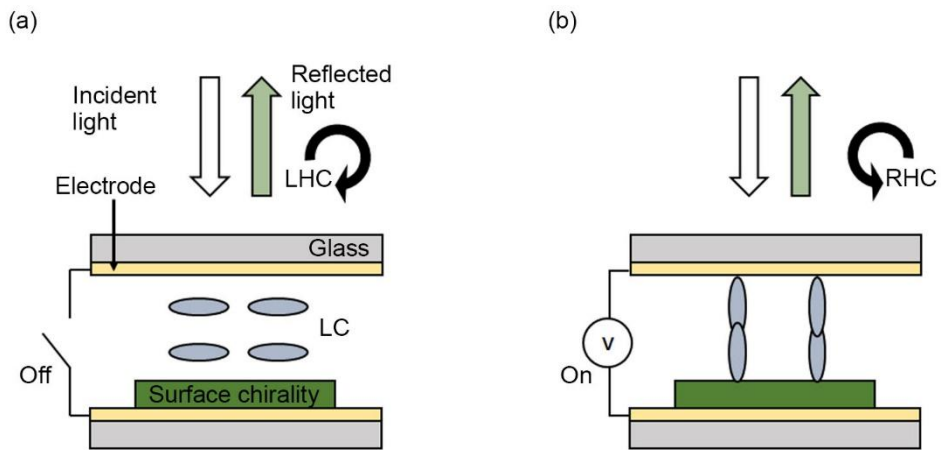


Figure 1.3 Schematic diagrams of the operation principles of the chiral surface-driven optical image selection by polarization: (a)

under no applied voltage and (b) in the presence of the applied voltage.

1.3 Outline of Thesis

This thesis consists of five chapters from Introduction to Conclusion. In Chapter 1, a general overview of the conventional image selection methods is provided. The brief description of the chiral surface-driven optical image selection and the operating principle of the polarization switching effect are also introduced in this chapter. Chapter 2 provides the theoretical background for understanding and numerically calculating the proposed concept, such as cholesteric LCs and chiral reactive mesogen (RM), Stokes parameters and Mueller matrix, nematic LCs as a tunable wave-retarder, and Berreman 4x4 propagation matrix method. Chapter 3 presents the experimental procedures of this research. The fabrication process through photo-polymerization of chiral RM, LC injection, and the characterization of the fabricated device are

covered as well in this chapter. In Chapter 4, the results of the simulation and the experiments are presented, compared, and discussed. Finally, in Chapter 5, some concluding remarks are made.

Chapter 2 Theoretical Background

2.1 Cholesteric Liquid Crystals and Chiral Reactive Mesogen

Cholesteric liquid crystal (CLC) is one of the phases in LCs. Nematic LCs form a twisted structure when chiral molecules (chiral dopants) are mixed. The director in each plane of the nematic LCs rotates about an axis that is perpendicular to the director plane as shown in Fig. 2.1. As the twisted structure continues, it becomes a helical photonic crystal, which consists a photonic band-gap. Due to this photonic band-gap, the CLC reflects certain range of wavelength. In addition, because of its rotating property (chirality), the CLC reflects a circularly polarized light. This reflection from a stratified structure is also called as Bragg reflection. The polarization type of the reflected light is determined depending on the handedness of the CLC. If the CLC is twisted in a right-handed direction, this CLC reflects a RHC light. On

the other hand, if the CLC is twisted in a left-handed direction, a LHC light is reflected from this CLC. The light that is not reflected by the CLC is all transmitted through the CLC.

The reflection peak (λ_p) and the bandwidth of the reflectance ($\Delta\lambda$) are determined by the pitch of the CLC (p) and the refractive indices of the LCs (n_o : ordinary refractive index, n_e : extraordinary refractive index, $\Delta n = n_e - n_o$). The equations between each variables are expressed as the following.

$$\lambda_p = \frac{n_e + n_o}{2} \cdot p \quad (2.1)$$

$$\Delta\lambda = \Delta n \cdot p \quad (2.2)$$

As we can see in these equations, the pitch of the CLC, which is determined by the helicity power of the chiral dopants, is the main factor of the reflected color. With higher helicity power, the pitch gets shorter, reflecting a blue-shifted color, and vice versa. In addition, the difference in the refractive indices of the LCs is directly connected with the bandwidth of the reflectance.

For an appropriate reflectance spectrum, an appropriate LC and chiral dopant concentration should be selected.

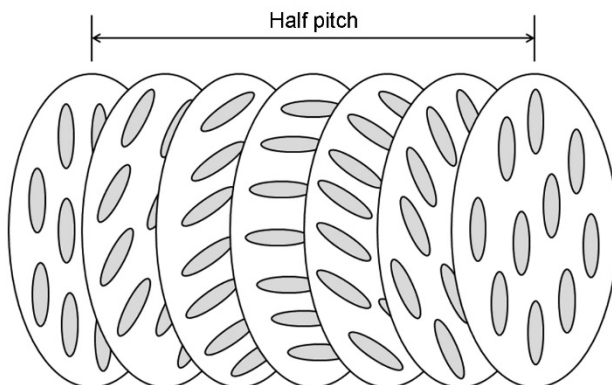


Figure 2.1 Schematic illustration of the CLC.

Generally, reactive mesogen (RM) is a type of polymerizable chemical compound with LC properties. As the RMs are polymerized by external stimuli such as heat or light, the RMs form a liquid crystalline polymer, which has high stability in heat and chemicals. The schematic diagram of the polymerization process of the RMs is depicted in Fig. 2.2. Since the LCs are affected by temperature, mechanical strength, and chemicals, liquid crystalline polymer has a great potential to overcome these

problems with same optical properties of LCs. In addition, the RMs can be dissolved in various solvents, which we call RM solution (RMS). With RMS, the fabrication process of such liquid crystalline polymer can be more simplified, such as spin-coating or dip-coating. With the simplified fabrication process, the RMS has greater potential for various applications.

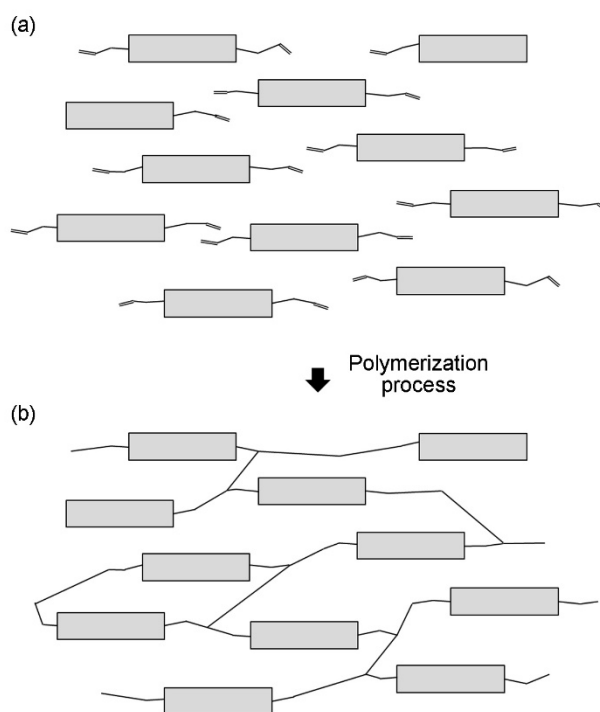


Figure 2.2 The schematic diagram of (a) the RMs and (b) the liquid crystalline polymer formed through the polymerization of RMs.

The chiral RM is a type of RM with the same optical properties of CLC. The chiral dopant in the RM produces the helicity power to the RMs, which has the ability to construct a helical photonic crystal. By dissolving the chiral RMs into a solvent, forming RMS, surface chirality can be easily achieved with simple fabrication process. This helical photonic crystal reflects circularly polarized light, which is same as the CLC. With surface chirality, simple structure dealing with circularly polarized light can be developed.

2.2 Stokes Parameters and Mueller Matrix

The polarization state of light can be represented by various methods. Within those methods, the Stokes parameters can describe the polarization state better than others can. The Stokes vector, comprised with the Stokes parameters, is usually used due to the full expression of the polarization and even unpolarized state, and the easy calculation with Mueller matrix. The

Stokes vector, \vec{S} , has 4 parameters as the following equation.

$$\vec{S} = \begin{bmatrix} S_0 \\ S_1 \\ S_2 \\ S_3 \end{bmatrix} \quad (2.3)$$

Here, S_0 denotes the time averaged total intensity of the light, regardless of its polarization. The other parameters, S_1 , S_2 , and S_3 , denotes the relative intensity of the horizontal, $+45^\circ$, and the RHC light, respectively. The parameters representing the polarization state (S_1 , S_2 , and S_3) can be any real number between -1 and 1. If these parameters have negative values, this means that the polarization state of light consists the orthogonal polarization with respect to the positive value. For example, if S_3 is negative, it represents the light having a LHC composition. The advantage of Stokes vector over Jones vector is that while the Jones vector can only represent full polarized light, the Stokes vector can express partially polarized, and even unpolarized light. When the light is unpolarized, the Stokes parameters are simply given as $S_0 > 0$, and $S_1 = S_2 = S_3 = 0$. For partially polarized light,

the relationship between Stokes parameters is $S_0^2 > S_1^2 + S_2^2 + S_3^2$. The relationship $S_0^2 > S_1^2 + S_2^2 + S_3^2$ is finally formed when the light is fully polarized. The Stokes vector for various polarization states are shown in Table 2.1.

Table 2.1 Stokes vector for various polarization states.

Polarization state		Stokes vector
Linear polarization	Horizontal	$[1 \ 1 \ 0 \ 0]^T$
	Vertical	$[1 \ -1 \ 0 \ 0]^T$
	+45°	$[1 \ 0 \ 1 \ 0]^T$
	-45°	$[1 \ 0 \ -1 \ 0]^T$
Circular polarization	RHC	$[1 \ 0 \ 0 \ 1]^T$
	LHC	$[1 \ 0 \ 0 \ -1]^T$

The polarization state modified by optical devices can be calculated with Mueller matrix. The calculation between the Stokes vector is done by

Mueller matrix. Mueller matrix was developed in 1943 by Hans Mueller. In contrast to the usage of 2x2 matrix method for Jones calculus, Mueller matrix uses an expanded 4x4 method to overcome the drawbacks of the Jones calculus. By simply multiplying the matrices to the Stokes vector, the polarization state of the output light from several optical elements can be calculated. The Mueller matrix for commonly used optical elements are shown in Table 2.2.

Table 2.2 Mueller matrices for common optical elements.

Optical elements		Mueller matrix
Linear polarizer	Horizontal transmission	$\frac{1}{2} \begin{bmatrix} 1 & 1 & 0 & 0 \\ 1 & 1 & 0 & 0 \\ 0 & 0 & 0 & 0 \\ 0 & 0 & 0 & 0 \end{bmatrix}$
	Vertical transmission	$\frac{1}{2} \begin{bmatrix} 1 & -1 & 0 & 0 \\ -1 & 1 & 0 & 0 \\ 0 & 0 & 0 & 0 \\ 0 & 0 & 0 & 0 \end{bmatrix}$
	+45° transmission	$\frac{1}{2} \begin{bmatrix} 1 & 0 & 1 & 0 \\ 0 & 0 & 0 & 0 \\ 1 & 0 & 1 & 0 \\ 0 & 0 & 0 & 0 \end{bmatrix}$

	-45° transmission	$\frac{1}{2} \begin{bmatrix} 1 & 0 & -1 & 0 \\ 0 & 0 & 0 & 0 \\ -1 & 0 & 1 & 0 \\ 0 & 0 & 0 & 0 \end{bmatrix}$
Circular polarizer	RHC	$\frac{1}{2} \begin{bmatrix} 1 & 0 & 0 & 1 \\ 0 & 0 & 0 & 0 \\ 0 & 0 & 0 & 0 \\ 1 & 0 & 0 & 1 \end{bmatrix}$
	LHC	$\frac{1}{2} \begin{bmatrix} 1 & 0 & 0 & -1 \\ 0 & 0 & 0 & 0 \\ 0 & 0 & 0 & 0 \\ -1 & 0 & 0 & 1 \end{bmatrix}$

2.3 Nematic Liquid Crystals as a Tunable Wave Retarder

The nematic LCs can be used as a wave retarder due to the optical anisotropy. As the extraordinary and ordinary refractive indices change the speed of the light according to the axis, the light passing through the nematic LC layer experiences wave retardation. In addition, with a constant thickness of the LC layer, the alignment of the LC can be shifted according to the applied voltage. As the alignment of the LC gets vertical, the amount of the phase retardation decreases, eventually becoming an isotropic layer to the

vertically incident light. Here, we are going to calculate the polarization state of the RHC light passing through the nematic LC layer acting as a tunable wave retarder. The Stokes vector of the RHC light is represented as P_0 . The Stokes vector P_0 is $[1 \ 0 \ 0 \ 1]^T$. Let us assume the phase retardation of the LC layer is symbolized as Φ . The Mueller matrix for the LC layer (M_1) is described as

$$M_1 = \begin{bmatrix} 1 & 0 & 0 & 0 \\ 0 & 1 & 0 & 0 \\ 0 & 0 & \cos\Phi & -\sin\Phi \\ 0 & 0 & \sin\Phi & \cos\Phi \end{bmatrix}. \quad (2.4)$$

The Stokes vector for the RHC light passed through the LC layer (P_1) is then described as

$$P_1 = M_1 P_0 = \begin{bmatrix} 1 \\ 0 \\ -\sin\Phi \\ \cos\Phi \end{bmatrix}. \quad (2.5)$$

We can see that the polarization state of the light changes as the alignment of the LCs changes. If we assume that the LC layer acts as a half-wave retarder

($\Phi = \pi$), the Stokes vector becomes $[1 \ 0 \ 0 \ -1]^T$, meaning that the light becomes LHC. When the alignment of the LC becomes vertical, the phase retardation becomes zero. With this condition, the Stokes vector becomes $[1 \ 0 \ 0 \ 1]^T$, which means, as expected, the light does not experience any phase retardation from the LC layer. This means that depending on the applied voltage, the polarization can be switched by the LC layer.

2.4 Berreman 4x4 Propagation Matrix Method

Electromagnetic wave propagation in stratified media is important in several applications like ellipsometry analysis, Bragg mirrors, or CLC structures. Propagation of plane waves in isotropic media can be solved with 2x2 propagation matrix methods. However, propagation of plane waves in anisotropic layers cannot be solved with this method. In the case of anisotropic layers, a 4x4 propagation matrix method was developed by Berreman in 1971 [23]. This method is now known as Berreman's 4x4

propagation matrix method.

As our surface chirality layer is comprised of CLC structures, the Berreman's 4x4 propagation matrix method is needed to calculate the reflecting property of our circularly polarized images. The Berreman's 4x4 propagation matrix method can be simply explained as the following.

First, we make a 6x6 matrix multiplying with a 1x6 matrix with all of the x , y , and z components in Maxwell's equations with the curl operator, ignoring the nonlinear optical effects. By assuming that the plane waves are incident obliquely in the x, z plane on a region in which the anisotropic layers are a function only of z , we can derive two linear algebraic equations from the multiplication of the 6x6 matrix and the 1x6 matrix. By substituting these two equations into others, we can eliminate two variables in the 1x6 matrix, getting four first-order linear differential equations. These four equations can be written in 4x4 matrix form. Since this matrix equation is a differential equation according to z , we can achieve the changes in the four elements of electric fields and magnetic fields of the light as it propagates along the z

direction. Berreman used a simple approximation for the calculation because solving the exact differential equations was impossible. Instead of calculating the differential equations, this method divided the continuous anisotropic layer into a summation of discrete anisotropic layers. With this approximation, the light propagation in such CLC structures can be calculated, and even the transmittance and the reflectance of these structures can be calculated.

To testify our modified simulation code which is based on the Berreman's 4x4 propagation matrix method, we fabricated CLC structures with various pitches. In addition, we fabricated stacked CLC structures and compared with the simulation result to verify whether the simulation code is correct or incorrect. These CLC structures on a substrate will be called as surface chiral layers. First, for the initial alignment and the adhesion for the RMS, the homogeneous alignment layer of polyimide (SE-6514H; Nissan Chemical Industries, Ltd.) was spin-coated on the surface of a glass substrate at the rate of 2000 rpm for 30 s. The alignment was post-annealed at 180 °C for 1 hr. For the alignment of the RMS, the substrate was homogeneously

rubbed. We used various mixtures of RMS (RMS11-066, RMS11-067, RMS11-068; Merck) and RM (RM257; Merck) for surface chiral layers with different pitches. Here, we prepared 6 distinct types of surface chiral layers. For the blue colored surface chiral layers, we mixed RMS11-066 and RMS11-067 at 4:6 and 2:8 weight ratio, named as B1 and B2, respectively. For the green colored Surface chiral layers, RMS11-067 and RMS11-068 were mixed at 7.5:2.5 and 5:5 weight ratio, named as G1 and G2, respectively. Lastly, for the red colored Surface chiral layers, RM257 was dissolved in RMS11-068 with the concentration of 3.8 wt.% and 5.8 wt.%, named as R1 and R2, respectively. Since these RMS are different only on their chiral dopant concentration, the pitch of the blended RMS and the wavelength. Also, since the reflection peak of RMS11-068 itself showed shorter wavelength than the required color, RM was additionally mixed to this solution to reduce the chiral dopant concentration. These mixtures were independently spin-coated on the glass substrates at the rate of 2000 rpm for 30 s. These were baked again at 75 °C for 1 min, rested at room temperature for 1 min, and polymerized by the

exposure of ultraviolet light (UV) at the intensity of 20 mW/cm² for 1 min.

The reflectance spectra of these Surface chiral layers were examined with a spectrometer (USB2000+; Ocean Optics).

For the simulation parameters, the extraordinary and the ordinary refractive indices were 1.67 and 1.54, respectively. The pitch lengths of each Surface chiral layers are shown in Table 2.3. As shown in Table 2.3, Surface chiral layers with longer reflecting wavelength have longer pitch.

Table 2.3 Simulation pitch lengths for each surface chiral layers.

Mixture	B1	B2	G1	G2	R1	R2
Pitch (nm)	0.275	0.295	0.32	0.34	0.41	0.445

The reflection peak wavelengths for each mixture in the simulation ($\lambda_{p,sim}$) and the experimental ($\lambda_{p,exp}$) results are shown in Table 2.4. The difference between the reflection peak of the simulation and the experimental results can be reduced by modifying the pitch length of the simulation

parameter since the exact experimental parameters of these RMS are unknown.

As shown in Fig. 2.3 and Fig. 2.4, the simulation result and the experiment result matches well.

Table 2.4 Peak wavelengths for each surface chiral layers

Mixture	B1	B2	G1	G2	R1	R2
$\lambda_{p,sim}$ (nm)	442	477	516	550	662	711
$\lambda_{p,exp}$ (nm)	442	473	512	548	652	719

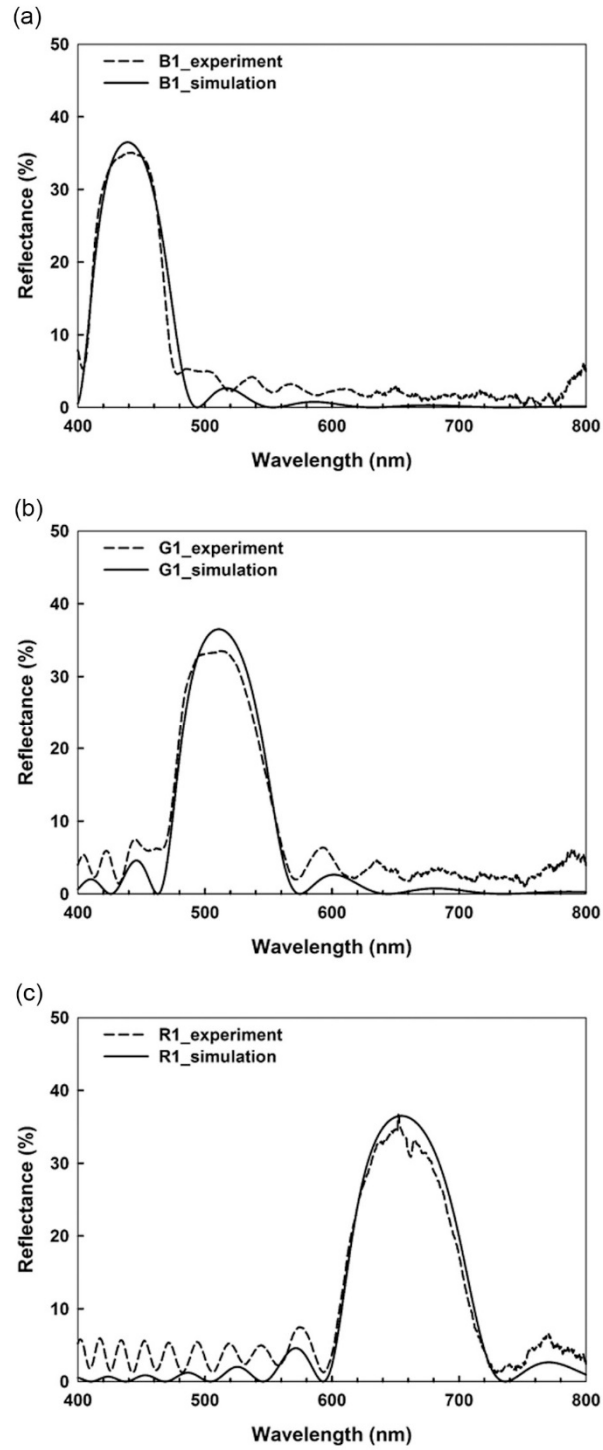


Figure 2.3 Experimental (dashed) and simulation (line) reflectance

spectra of (a) B1, (b) G1, and (c) R1.

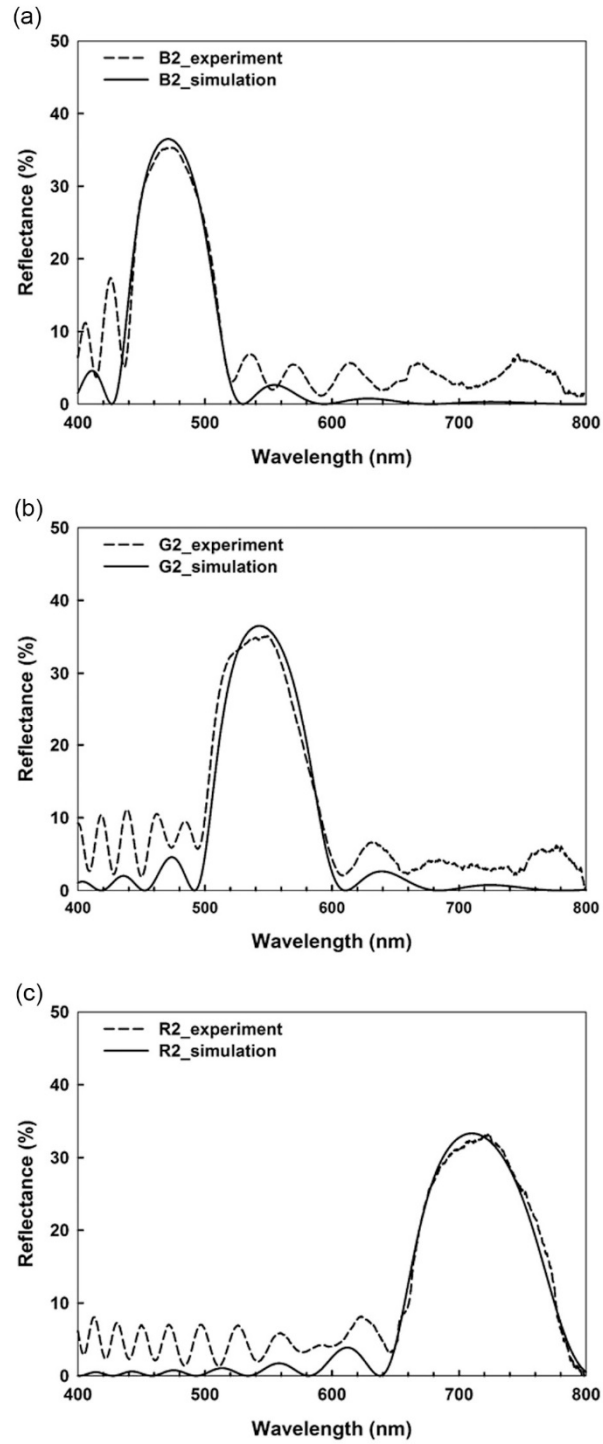


Figure 2.4 Experimental (dashed) and simulation (line) reflectance

spectra of (a) B2, (b) G2, and (c) R2.

With these RMS, stacked surface chiral structures were fabricated. To fabricate such structure, the homogeneous alignment layer was again prepared on the surface chiral layer fabricated above (B1, G1, and R1) at the same spin-coating rate. After post-annealing the alignment layer, the other RMS were prepared on the above structure (B2 on B1, G2 on G1, and R2 on R1). The substrates were baked and rested again, and the RMS were polymerized with the UV exposure. The schematic of the stacked surface chiral structure is depicted in Fig. 2.5.

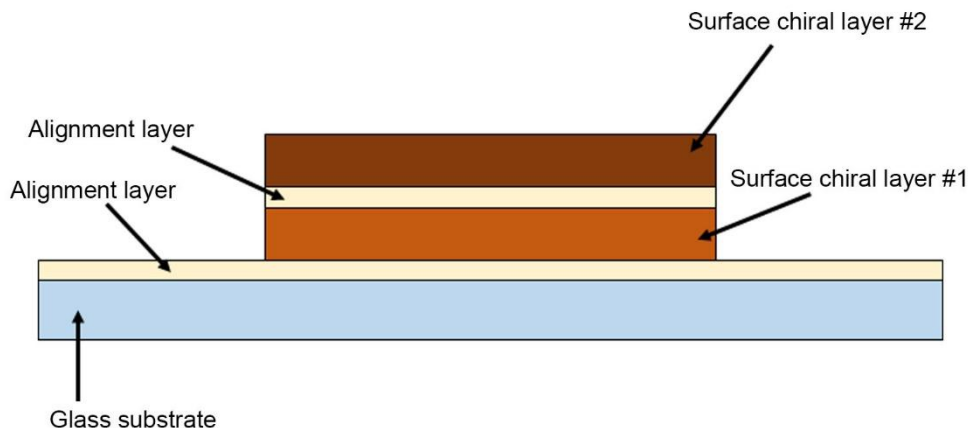


Figure 2.5 Schematic diagram of the stacked surface chiral structure.

Surface chiral layer #1 is B1, G1, or R1, and surface chiral layer #2 is B2, G2, or R2, respectively.

The reflectance property of these stacked surface chiral structures was again examined with the spectrometer. Also, these structures were numerically calculated with the identical simulation code and parameters used above. The refractive index of the alignment layer was 1.5 and the thickness of the alignment layer was 100 nm. The reflectance spectra of these structures are shown in Fig. 2.6.

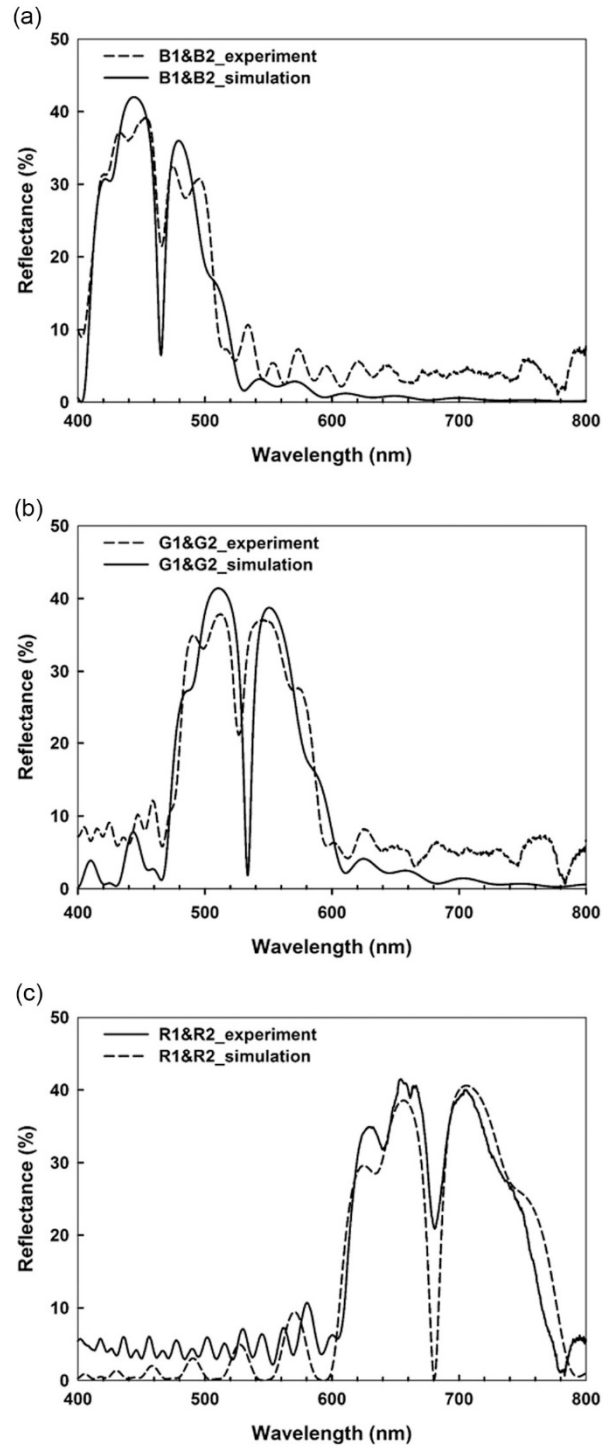


Figure 2.6 Experimental (dashed) and simulation (line) reflectance

spectra of stacked surface chiral structures consisted of (a) B1&B2, (b) G1&G2, and (c) R1&R2.

Both on experimental results and the simulation results, the reflection band became broader than the single surface chiral layer due to the different pitches in the stacked structures. Also, the maximum reflectance is higher in the stacked structure than the single structure due to more number of pitches. In these reflectance spectra, however, the reflectance is decreased tremendously at a certain wavelength. The position of these decreased valleys is almost the position where the maximum reflectance should be. These valleys are formed due to the alignment layer, acting as a defect layer, between the surface chiral layers. It is well known that defect within the photonic crystals traps light. Since surface chiral layer is a type of photonic crystals, the alignment layer between the surface chiral layers becomes a defect layer between the photonic crystals. If the reflectance spectra of the bottom and the top surface chiral layers did not overlap each other, such

valley would not be formed. Since the reflectance spectra of two surface chiral layers overlap, such valley was formed. To explain this phenomena more easily, it can be thought that the reflected light from the bottom surface chiral layer is again reflected back from the top surface chiral layer, and this process occurs iteratively, eventually trapped inside the alignment layer. These results about defects in CLCs are also showed in previous studies [24].

With the results above, the simulation code was verified and the simulation code can be said that it performs well in stratified structures.

Chapter 3 Experiments

3.1 Patterned Indium–Tin–Oxide (ITO) Substrate

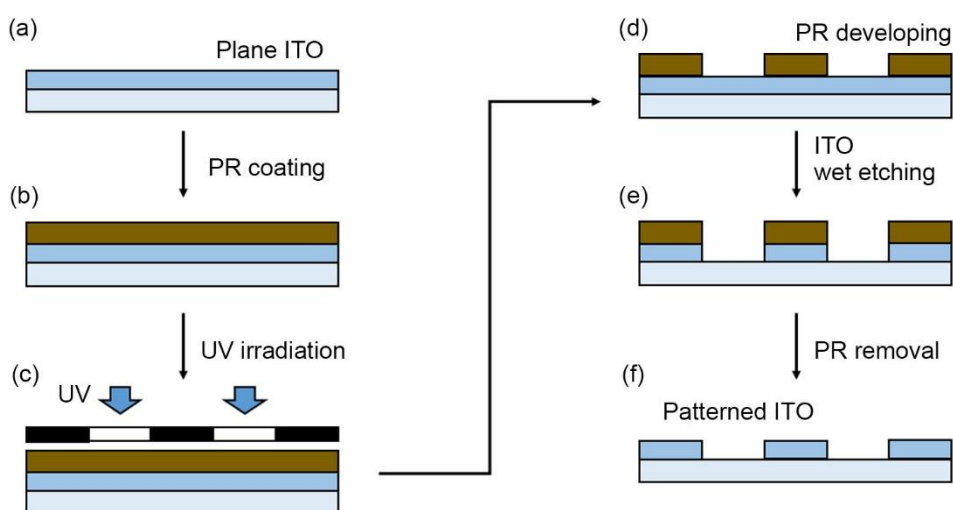


Figure 3.1 Fabrication process of isolating ITO pixels: (a) Plane ITO

substrate. (b) PR spin-coating on the ITO substrate for etching mask.

(c) UV exposure for patterning PR. (d) Developing PR. (e) Wet etching ITO. (f) Removing the PR.

For the isolated control of each surface chiral images, the electrode

should be disconnected to each other. Figure 3.1 depicts the fabrication process of the isolating each ITO pixels. A plane ITO substrate was pixelated with photolithography (Fig. 3.1(a)). Photoresist (PR; AZ 5412 E; MicroChemicals) was prepared on the plane ITO substrate at the rate of 2000 rpm for 30 s with spin-coating (Fig. 3.1(b)). PR layer was post-annealed at 95 °C for 210 s. The annealed PR was exposed to UV light at the intensity of 20 mW/cm² for 5 s (Fig. 3.1(c)). For the positive PR property, the substrate was baked at 110 °C for 2 min. After leaving the substrate at room temperature for 3 min, the PR was exposed to UV light with the same intensity as above for 25 s. Then, the PR was developed for 35 s by a developer solution (AZ 300; Merck) (Fig. 3.1(d)). Using the patterned PR as an etching mask, the ITO was wet etched for 10 min by the ITO etchant (Fig. 3.1(e)). By removing the PR by sonicating in acetone (Chemitop Co., Ltd) for 5 min, pixelated ITO substrate was achieved (Fig. 3.1(f)).

3.2 Preparation of Surface Chiral Images

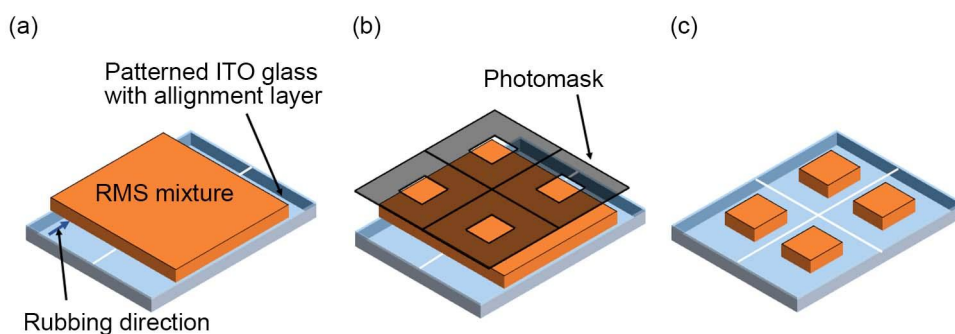


Figure 3.2 Fabrication process of the patterned surface chiral images:

(a) Preparation of surface chiral layer through spin-coating RMS mixture on a patterned ITO glass with alignment layer. (b) Patterned photo-polymerization through UV exposure. (c) Washout process of unpolymerized RMS.

Figure 3.2 shows the fabrication process of the surface chiral images.

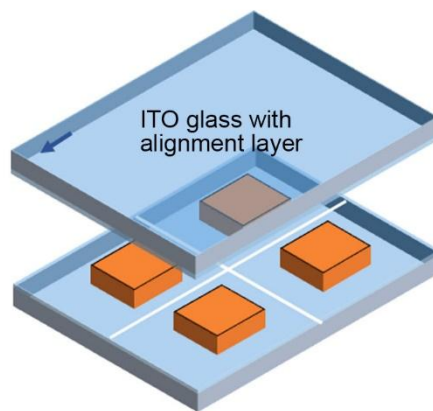
The homogeneous alignment layer of polyimide (SE-6514H; Nissan Chemical Industries, Ltd.) was spin-coated on inner surface of the indium-tin-oxide (ITO) patterned glass substrates at the rate of 2000 rpm for 30 s. The

alignment layer was post-annealed at 180 °C for 1 hr. For the initial alignment of the surface chiral layer and LC, the top and bottom substrates were anti-parallelly rubbed. On the bottom substrate, the surface chiral layer was fabricated with chiral reactive mesogen solutions (RMS). Chiral RMS (RMS11-067, RMS11-068; Merck) were blended at 6.5:3.5 weight ratio to achieve the reflection peak (λ_p) at 550 nm. The RMS mixture was deposited at the rate of 2000 rpm for 30 s as shown in Fig. 3.2(a). The substrate was baked again at 75 °C for 1 min for the proper alignment of the chiral RMS, and was rested at room temperature for 1 min. With a photomask, the coated chiral RMS was polymerized by the exposure of ultraviolet light (UV) at the intensity of 20 mW/cm² for 1 min as shown in Fig. 3.2(b). The UV-exposed part of the chiral RMS became the surface chiral layer. The un-polymerized part of the chiral RMS was washed by toluene and acetone, and the substrate was dried at 75 °C for 1 min to evaporate the residual acetone. Here, toluene was chosen as the washing solution because the solvent of the chiral RMS is toluene. After the washing process, only the patterned surface chiral layer

remained as shown in Fig. 3.2(c).

3.3 Fabrication of Polarization Switchable LC Cell

(a)



(b)

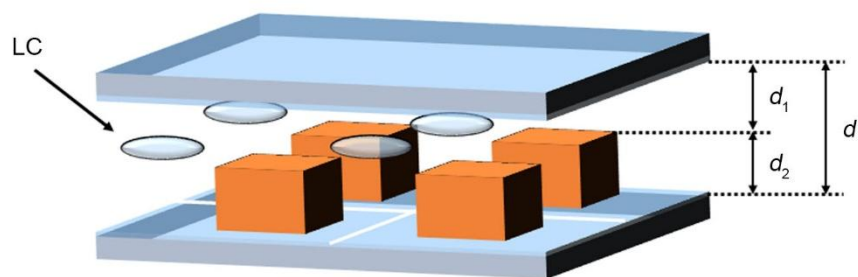


Figure 3.3 Fabrication process of the LC cell: (a) Assembling a cell

with anti-parallel rubbing direction of the bottom and the top substrate. (b) Injection of LC in the cell through capillary action.

For the tunable wave retarder, the LC cell have been fabricated as shown in Fig. 3.3. The surface chiral image substrate and the ITO substrate with alignment layer were assembled as shown in Fig. 3.3(a). A nematic LC (E7, $n_o = 1.5216$, $n_e = 1.7462$, $\Delta n = 0.2246$; Merck) was injected into the constructed cell by capillary action, as shown in Fig. 3.3(b). The cell gap (d) was maintained with glass fiber spacers of 3 μm thickness. The thickness of the LC layer (d_1) was determined by the cell gap and the height of surface chiral layer (d_2). d_2 , measured by a surface profiler (Alpha-step 200; KLA-TENCOR), was 1.8 μm , and thus d_1 became 1.2 μm . The relationship between the phase retardation and the thickness of the LC layer can be described as

$$\Gamma = \frac{2\pi}{\lambda_p} \Delta n d_1 \quad (3.1)$$

where Γ is the quantity of the retarded phase by the LC layer. In case of the half-wave retardation at the wavelength 550 nm, d_1 simply becomes 1.2 μm , which is identical with our fabricated device. According to the relationship above, different thickness of the LC layer is needed for different coloration. By controlling the spin-coating rate during the preparation of the chiral RMS, the thickness of the LC layer can be modified according to the different peak wavelength.

Chapter 4 Results and Discussion

4.1 Polarization Dependent Reflecting Properties of the Chiral Surface–Driven Optical Images in LC Devices

Let us first examine the reflectance spectra and the polarization state of our device. The simulation was based on Berreman 4×4 propagation matrix formulation. In the simulation, the helicity of the surface chiral layer was set as right-handed. We have designed the Bragg reflection light from the surface chiral layer to be the peak wavelength at 550 nm, which shows a green color. The ordinary and extraordinary refractive indices of the surface chiral layer were set as 1.52 and 1.75, respectively, and the pitch was set as 340 nm. The parameters of the LC were set identically with the parameters of E7, and the thickness of the LC layer was set as 1.2 μm . The experimental reflectance spectra were examined with a spectrometer (USB2000+; Ocean Optics)

The theoretical and experimental reflection spectra with no filter, RHC filter, and LHC filter are shown in Fig. 4.1. Fig. 4.1(a) shows the reflection spectra with no optical filter. Even with the variation in the voltage, which directly affects the alignment of the LC, the reflection spectrum does not change. This is because without a filter, the modification in the polarization state of the reflected light cannot be detected. Note that the reflectance of our device at 550 nm (35 %) is lower than usual cholesteric LCs (CLCs) [25-29]. It is well known that more than 10 pitches shows full reflection [30]. In our case, the surface chiral layer is only 1.8 μm thick, which contains only about 6 pitches. The lack of pitches can cause the band gap of the photonic crystal to be imperfect, eventually having deficiency in its reflectance. In the case of the RHC filter as shown in Fig. 4.1(b), green color with 35 % reflectance is obtained at 1.9 V (on-state) while nearly 0 % reflectance is obtained at 0 V (off-state). On the contrary, with the LHC filter as shown in Fig. 4.1(c), almost 0 % reflectance is obtained at the ‘on-state’ while green color with 35 % reflectance is obtained at the ‘off-state’. The

microscopic images for each condition are shown in the insets of Fig. 4.1, taken by a polarizing optical microscopy (Eclipse E600; Nikon). This result clearly shows that our device produces switchable orthogonal circularly polarized lights, controlled by the applied voltage.

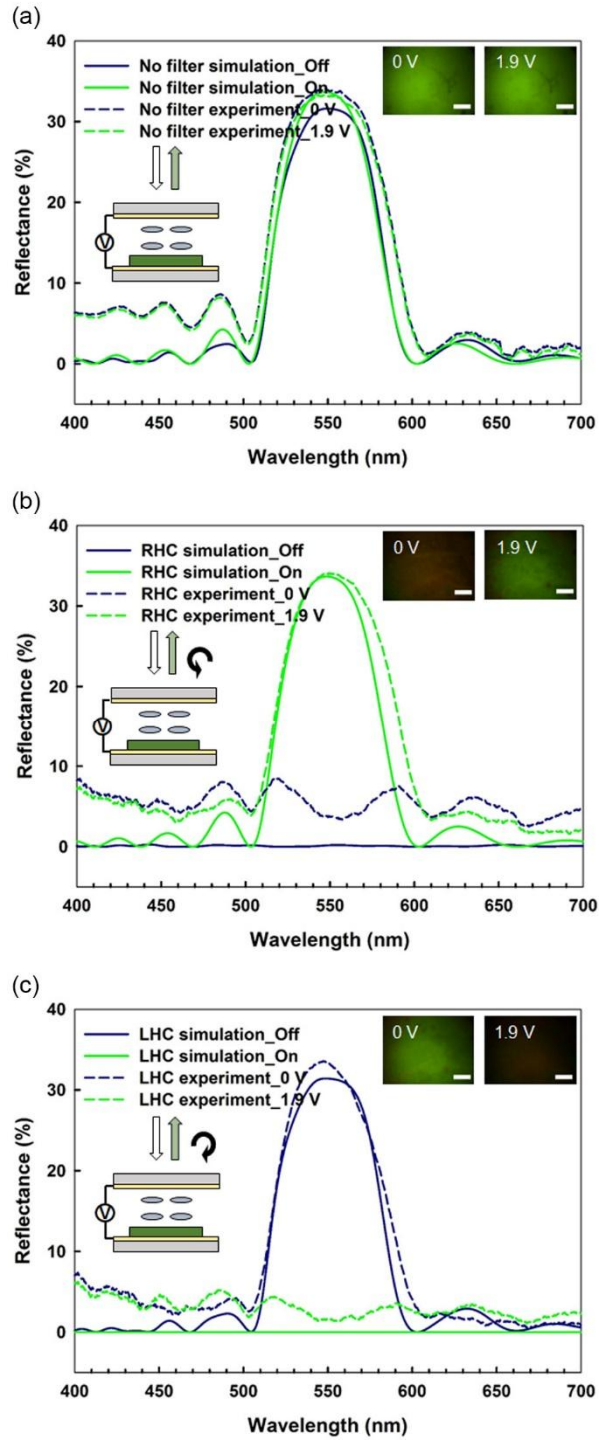


Figure 4.1 Theoretical and experimental reflection spectra according

to the applied voltage and the filter type. Reflection spectra with (a) no filter, (b) RHC filter, and (c) LHC filter. The upper-right insets in all figures show the microscopic images of our device depending on the applied voltage. Scale bars represent 500 μm .

4.2 Electro–optical Characteristics of the Chiral Surface–Driven Optical Images in LC Devices

The simulation result and the experimental result of the polarization state of our device as a function of the applied voltage are shown in Fig. 4.2. The simulation was conducted with a commercial program (LCD Master; Shintech). Here, we use the Stokes parameter, which is explained at Chapter 2. In particular, we mainly focus on the fourth parameter, S_3 , which expresses the degree of circular polarization. S_3 can be any real number between -1 (perfectly LHC) and 1 (perfectly RHC). We achieved the experimental S_3 value by estimating the ratio between the difference of RHC and LHC

reflectance and the summation of RHC and LHC reflectance. As shown in Fig. 4.2(a), S_3 of the light reflected from our device changes from -0.87 to 0.87 with increment of the applied voltage, meaning that the light reflected from our device changes its polarization state from LHC to RHC. This is due to the electro-optical property of the LC. Since the LC we used has positive dielectric anisotropy ($\Delta\epsilon > 0$), the director of our LC tries to align parallel with the applied electric field. Since the applied electric field of our device is perpendicular to the substrate, the director of our LC gradually changes its direction perpendicular to the substrate as the applied voltage gets higher. When the LC aligns perfectly perpendicular to the substrate, the LC layer loses its ability as a wave-retarder, being isotropic to the incident light. The tunable RHC and LHC reflectance peaks depending on the applied voltage are depicted in Fig. 4.2(b). As expected, the RHC reflectance gradually increases with higher voltage while the LHC reflectance shows the reversed property. The anchoring variation can cause the difference between the simulation and the experimental result.

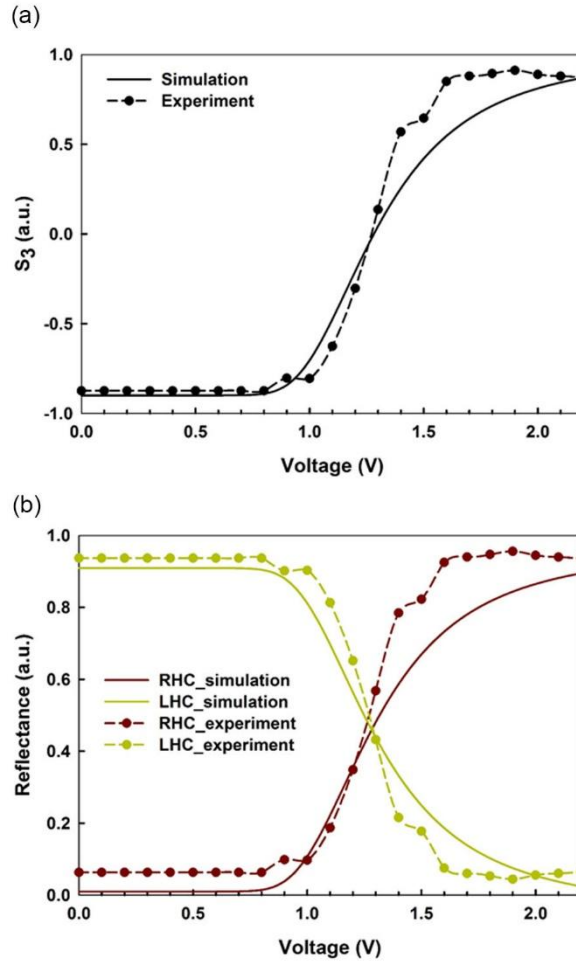


Figure 4.2 The numerical and experimental electro-optical properties of our device. (a) The Stokes parameter, S_3 as a function of applied voltage. (b) The reflectance with simulation RHC filter (red line), experiment RHC filter (red dot), simulation LHC filter (yellow line), and experiment LHC filter (yellow dot) as a function of voltage.

4.3 Surface Chiral Images with Different Helical Pitch in Chiral RM Layer

The patterned surface chiral layer with different colors are depicted in Fig. 4.3. Fig. 4.3(a)-(c) shows the device with green coloration surface chirality, and Fig. 4.3(d)-(f) shows the device with the blue coloration surface chirality. Here, another chiral RMS (RMS11-066; Merck) was blended with RMS11-067 at the weight ratio of 4:6 for the blue reflecting surface chirality. This mixture was spin-coated with a slower rate, 1500 rpm, than the green coloration surface chirality. With slower spin-coating rate, we could achieve a thicker surface chiral layer, which makes the thickness of the LC layer thinner to satisfy the half-wave retarder for blue color under equal cell gap. Viewing our devices with no filter, as shown in Fig. 4.3(a) and (d), all of the patterned surface chiral layer reflects their color even with the applied voltage. As we view our devices with RHC filter and LHC filter, our devices reflect their

color patterns according to the applied voltage. To be specific, since the voltage is applied on the left side, the patterns on the right side are selected by the RHC filter (Fig. 4.3(b) and (e)), and the patterns on the left side are selected by the LHC filter (Fig. 4.3(c) and (f)). This indicates that our device can be fabricated with different color patterned surface chiral layer in one device.

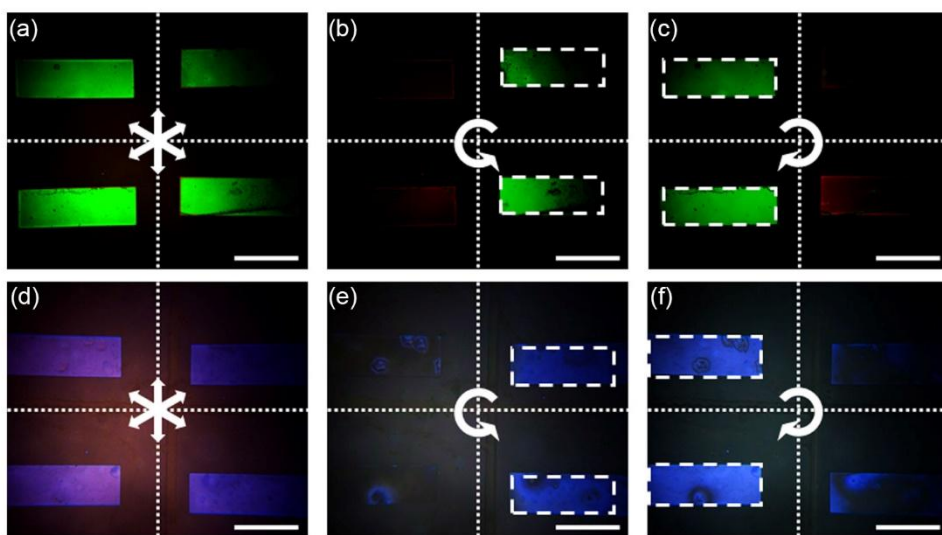


Figure 4.3 The microscopic images with different pitch length in the surface chiral pixel. The pixels are prepared with (a)-(c) green coloration and (d)-(f) blue coloration. The voltage was applied identically on the left pixels. Reflection through no filter with (a)

green and (d) blue coloration, RHC filter with (b) green and (e) blue coloration, and LHC filter with (c) green and (f) blue coloration are shown. Scale bar are 500 μm .

4.4 Switching Capability with Pixelated Surface Chiral Images

The polarization switching effect of our 2×2 pixel patterned surface chiral layer according to the applied voltage to each pixel is shown in Fig. 4.4.

Fig. 4.4(a)-(c) show the voltage applied 2×2 pixels viewing through the RHC filter, and Fig. 4.4(d)-(f) show the same voltage applied 2×2 pixels viewing through the LHC filter. On the voltage map, depicted in Fig. 4.4, the pixels with applied voltage are symbolized as '1', and '0' symbolizes the pixels with no voltage. Here, the voltage was applied in three separate ways. First, the voltage was applied on just one pixel, the second quadrant pixel (Fig. 4.4(a) and (d)). With the RHC filter (Fig. 4.4(a)), the green color only from the second quadrant pixel was visible, while the others were not. On the contrary,

we achieved three green coloration pixels with the LHC filter (Fig. 4.4(d)).

Second, the voltage was applied on two diagonal pixels, the second and the fourth quadrant pixel (Fig. 4.4(b) and (e)). A one-sided diagonal shape was formed through the RHC filter (Fig. 4.4(b)), while the formation of an opposite-sided diagonal shape was achieved with the LHC filter (Fig. 4.4(e)).

Lastly, all of the pixels except the first quadrant pixel were applied with the voltage (Fig. 4.4(c) and (f)). Only the first quadrant pixel remained dark when we viewed with the RHC filter (Fig. 4.4(c)). On contrast, the first quadrant pixel only showed its green coloration through the LHC filter (Fig. 4.4(f)).

This result clearly shows that our device can easily switch the polarization of reflected light to the opposite circular polarization through voltage even in pixel structure.

Theoretically, the pixels should show no reflection when the polarization state of the reflected light and that of the filter are orthogonal to each other. However, some pixels in Fig. 4.4 show such leakage on their edges. This can be explained by the distortion of LC alignment near the pixel edges.

Since the surface chiral pixel gives a squared protruding structure in the LC cell, the LCs around the pixel boundaries align differently with the majority of LCs. The protrusion alters the pretilt angle around the boundaries, eventually showing unintended reflection from dark pixels. To reduce this leakage, studies such as giving molecular ordering to the protrusion to eliminate pretilt variation can be applied to our device for better quality [31].

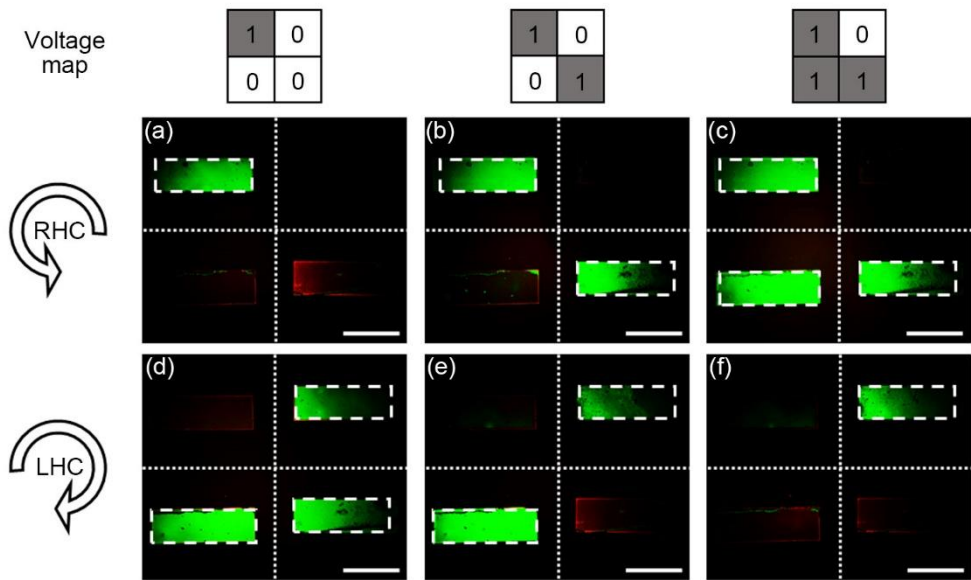


Figure 4.4 The microscopic images of the switching ability through the applied voltage on each pixels viewed through the (a)-(c) RHC

filter and the (d)-(f) LHC filter. The voltage maps on the pixels are shown on the top of the images. Scale bars are 500 μm .

4.5 Optical Image Selection by Polarization

We now assess the orthogonally polarized image selection of our concept. For orthogonally polarized image selection, the word ‘SNU’ and ‘MIPD’ were patterned with green coloration surface chirality as shown in Fig. 4.5(a). As we described, the circularly polarized state can be modified with the applied voltage. Here, we targeted the polarization state of the word ‘SNU’ to be RHC, and the word ‘MIPD’ to be LHC. To accomplish this condition, we applied the voltage at the upper side of the device, where the word ‘SNU’ is inscribed, and applied no voltage at the lower side of the device, where the word ‘MIPD’ is inscribed. Since the LCs in the upper side are aligned perpendicular to the substrate due to the applied voltage, the word ‘SNU’ is reflected with a perfect RHC state. In contrast, because the LCs in the lower

side of the device are aligned parallel to the substrate, the word ‘MIPD’ is reflected with a perfect LHC state. With the RHC and LHC filter, the desired image can be selected, as shown in Fig. 4.5(b) and (c), respectively. With our device, image selection by orthogonally tunable polarization was achieved. Here, we only just featured a limited number of pixels or images. However, with the expansion in the area of the substrate and increment in the number of pixels with red, green, and blue colors, our device can present symbols, images, or even videos created by these pixels with orthogonal circularly polarized lights.

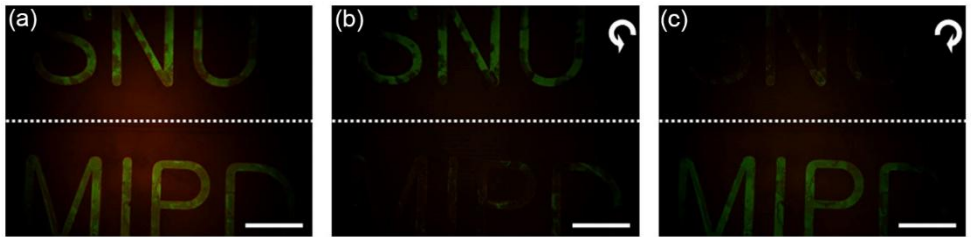


Figure 4.5 Image selection with orthogonal circular polarizers. (a)

The surface chiral layer was patterned with the word ‘SNU’ and ‘MIPD’. The voltage was applied on the upper side, where the word

‘SNU’ is inscribed. Only the word (b) ‘SNU’ was retrieved through the RHC filter, and the word (c) ‘MIPD’ was retrieved through the LHC filter. Scale bars are 500 μm .

Chapter 5 Conclusion

In this thesis, a new concept of a chiral surface-driven optical images in LC devices for optical image selection was proposed. The device was constructed simply with a polymerized chiral RMS and LC layer acting as a tunable phase retarder. The surface chiral images was constructed by the polymerized chiral RMS, where they reflect circularly polarized light depending on the chirality of their helical photonic crystals. Also, as LCs has electro-optical anisotropic properties, LC layer could change the polarization state from the surface chiral images and the voltage application had the ability to change the director alignment of the LCs. Depending on the applied voltage, the phase retardation from the LC layer can be modulated, and thus we can select RHC or LHC images. To be specific, with the voltage, the images could be constructed with RHC or LHC, and with the RHC or LHC filter, one could retrieve different images. Our device ensures perfect orthogonality and

switchable image selection. Also, with simple fabrication and construction in one cell unit, it is advantageous for practical applications. Our image selection device is expected to play a significant role in reflective-type 3D displays, color filters, and stealth technologies.

Bibliography

- [1] X. Li, J.W. Chon, S. Wu, R.A. Evans, M. Gu, “Rewritable polarization-encoded multilayer data storage in 2, 5-dimethyl-4-(p-nitrophenylazo) anisole doped polymer,” *Opt. Lett.* **32** (2007) 277-279.
- [2] D. McPhail, M. Gu, “Use of polarization sensitivity for three-dimensional optical data storage in polymer dispersed liquid crystals under two-photon illumination,” *Appl. Phys. Lett.* **81** (2002) 1160-1162.
- [3] H.H. Pham, I. Gourevich, J.K. Oh, J.E.N. Jonkman, E. Kumacheva, “A multidye nanostructured material for optical data storage and security data encryption,” *Adv. Mater.* **16** (2004) 516-520.
- [4] A.B. Taylor, P. Michaux, A.S. Mohsin, J.W. Chon, “Electron-beam lithography of plasmonic nanorod arrays for multilayered optical storage,” *Opt. Express* **22** (2014) 13234-13243.
- [5] P. Zijlstra, J.W. Chon, M. Gu, “Five-dimensional optical recording mediated by surface plasmons in gold nanorods,” *Nature* **459** (2009) 410-413.
- [6] W. Yue, S.S. Lee, E.S. Kim, “Angle-tolerant polarization-tuned color filter exploiting a nanostructured cavity,” *Opt. Express* **24** (2016) 17115-17124.
- [7] T. Ellenbogen, K. Seo, K.B. Crozier, “Chromatic plasmonic polarizers for active visible color filtering and polarimetry,” *Nano Lett.* **12** (2012) 1026-1031.

- [8] L. Duempelmann, D. Casari, A. Luu-Dinh, B. Gallinet, L. Novotny, "Color rendering plasmonic aluminum substrates with angular symmetry breaking," *ACS Nano* **9** (2015) 12383-12391.
- [9] H. Yun, S.Y. Lee, K. Hong, J. Yeom, B. Lee, "Plasmonic cavity-apertures as dynamic pixels for the simultaneous control of colour and intensity," *Nat. Commun.* **6** (2015) 7133.
- [10] E. Heydari, J.R. Sperling, S.L. Neale, A.W. Clark, "Plasmonic color filters as dual-state nanopixels for high-density microimage encoding," *Adv. Funct. Mater.* **27** (2017) 1701886.
- [11] X.M. Goh, Y. Zheng, S.J. Tan, L. Zhang, K. Kumar, C.W. Qiu, J.K. Yang, "Three-dimensional plasmonic stereoscopic prints in full colour," *Nat. Commun.* **5** (2014) 5361.
- [12] C.-T. Lee, H.-Y. Lin, C.-H. Tsai, "Designs of broadband and wide-view patterned polarizers for stereoscopic 3D displays," *Opt. Express* **18** (2010) 27079-27094.
- [13] W.T. Chen, K.Y. Yang, C.M. Wang, Y.W. Huang, G. Sun, I.D. Chiang, C.Y. Liao, W.L. Hsu, H.T. Lin, S. Sun, L. Zhou, A.Q. Liu, D.P. Tsai, "High-efficiency broadband meta-hologram with polarization-controlled dual images," *Nano Lett.* **14** (2014) 225-230.
- [14] H. Kim, J. Kim, J. Kim, B. Lee, S.-D. Lee, "Liquid crystal-based lenticular lens array with laterally shifting capability of the focusing effect for autostereoscopic displays," *Opt. Commun.* **357** (2015) 52-57.
- [15] H. Kang, S. Roh, I. Baik, H. Jung, W. Jeong, J. Shin, I. Chung, "A novel

- polarizer glasses-type 3D displays with a patterned retarder,” *S.I.D. Symp. Digest Tech. Pap.* **41** (2010) 1-4.
- [16] K.-S. Bae, U. Cha, Y.-K. Moon, J.W. Heo, Y.-J. Lee, J.-H. Kim, C.-J. Yu, “Reflective three-dimensional displays using the cholesteric liquid crystal with an inner patterned retarder,” *Opt. Express* **20** (2012) 6927-6931.
- [17] Y.J. Wu, Y.S. Jeng, P.C. Yeh, C.J. Hu, W.M. Huang, “Stereoscopic 3D display using patterned retarder,” *S.I.D. Symp. Digest Tech. Pap.* **39** (2008) 260-263.
- [18] Y. Cui, R.S. Hegde, I.Y. Phang, H.K. Lee, X.Y. Ling, “Encoding molecular information in plasmonic nanostructures for anti-counterfeiting applications,” *Nanoscale* **6** (2014) 282-288.
- [19] Y. Heo, H. Kang, J.S. Lee, Y.K. Oh, S.H. Kim, “Lithographically encrypted inverse opals for anti-counterfeiting applications,” *Small* **12** (2016) 3819-3826.
- [20] H. Hu, Q.-W. Chen, J. Tang, X.-Y. Hu, X.-H. Zhou, “Photonic anti-counterfeiting using structural colors derived from magnetic-responsive photonic crystals with double photonic bandgap heterostructures,” *J. Mater. Chem.* **22** (2012) 11048-11053.
- [21] Y. Liu, Y.H. Lee, Q. Zhang, Y. Cui, X.Y. Ling, “Plasmonic nanopillar arrays encoded with multiplex molecular information for anti-counterfeiting applications,” *J. Mater. Chem. C* **4** (2016) 4312-4319.
- [22] H. Ditlbacher, J. Krenn, B. Lamprecht, A. Leitner, F. Aussenegg, “Spectrally coded optical data storage by metal nanoparticles,” *Opt. Lett.*

25 (2000) 563-565.

- [23] D.W. Berreman, "Optics in stratified and anisotropic media: 4×4-matrix formulation," *J. Opt. Soc. Am.* **62** (1972) 502-510.
- [24] Y.-C. Hsiao, H.-T. Wang, W. Lee, "Thermodielectric generation of defect modes in a photonic liquid crystal," *Opt. Express* **22** (2014) 3593-3599
- [25] Y.-C. Hsiao, W. Lee, "Electrically induced red, green, and blue scattering in chiral-nematic thin films," *Opt. Lett.* **40** (2015) 1201-1203.
- [26] Y. Mohri, J. Kobashi, H. Yoshida, M. Ozaki, "Morpho-butterfly-inspired patterning of helical photonic structures for circular-polarization-sensitive, wide-angle diffuse reflection," *Adv. Opt. Mater.* **5** (2017) 1601071.
- [27] A.C. Tasolamprou, M. Mitov, D.C. Zografopoulos, E.E. Kriezis, "Theoretical and experimental studies of hyperreflective polymer-network cholesteric liquid crystal structures with helicity inversion," *Opt. Commun.* **282** (2009) 903-907.
- [28] M.E. McConney, V.P. Tondiglia, J.M. Hurtubise, L.V. Natarajan, T.J. White, T.J. Bunning, "Thermally induced, multicolored hyper-reflective cholesteric liquid crystals," *Adv. Mater.* **23** (2011) 1453-1457.
- [29] J.-D. Lin, C.-L. Chu, H.-Y. Lin, B. You, C.-T. Horng, S.-Y. Huang, T.-S. Mo, C.-Y. Huang, C.-R. Lee, "Wide-band tunable photonic bandgaps based on nematic-refilling cholesteric liquid crystal polymer template samples," *Opt. Mater. Express* **5** (2015) 1419-1430.
- [30] D.Y. Kim, C. Nah, S.W. Kang, S.H. Lee, K.M. Lee, T.J. White, K.U. Jeong, "Free-standing and circular-polarizing chirophotonic crystal

reflectors: photopolymerization of helical nanostructures,” *ACS Nano* **10** (2016) 9570-9576.

- [31] S.-U. Kim, B.-Y. Lee, J.-H. Suh, J. Kim, J.-H. Na, S.-D. Lee, “Reduction of gamma distortions in liquid crystal display by anisotropic voltage-dividing layer of reactive mesogens,” *Liq. Cryst.* **44** (2016) 364-371.

초록

최근에 빛의 편광 상태에 따라 다른 이미지를 보여주는 시스템 구현을 위한 다양한 방식들이 개발되어 왔다. 빛의 편광 상태에 따라 다른 이미지를 보여주는 시스템은 광학적 이미지 저장 시스템, 안경식 3차원 디스플레이, 그리고 위조 방지와 같은 다양한 분야에 응용되어 왔다. 기존 연구에서는 편광판을 통해 간단하게 이미지를 얻을 수 있고, 이미지 형성 시스템의 직관적인 구조 덕분에 선형 편광을 사용한 광학적 이미지 선택이 폭넓게 연구되어 왔다. 하지만 선형 편광을 사용하면 편광판과 이미지의 편광 상태가 완벽하게 정렬해야 원하는 이미지를 검출할 수 있는 단점이 존재한다. 예를 들어, 선형 편광을 이용한 3차원 디스플레이는 시청자가 올바른 자세에서 보지 않으면 3차원 이미지가 형성되지 않는다. 자세히 말해, 만약 시청자가 누워서 디스플레이를 본다면,

안경에 있는 편광판의 편광 방향과 3차원 디스플레이에서 형성되는 이미지의 편광 방향이 맞지 않아 3차원 이미지가 형성되지 않는다. 이러한 문제점들을 극복하기 위해 편광 방향이 존재하지 않는 원형 편광을 사용한 이미지 검출이 제시되어 왔다. 원형 편광을 얻기 위해서는 카이랄성 구조 혹은 위상 지연 소자가 사용되었다. 하지만 기존 연구들에서는 품질과 응용 분야 증대를 가능하게 할 수 있는 편광 상태를 반대로 바꾸는 기능에서 한계가 존재했다. 또한, 실제 사용 가능성을 위해 원형 편광 구조의 간단한 공정이 필요하다.

본 논문은 액정 장치에서의 편광을 통한 카이랄 표면 구동 이미지 선택 시스템을 제안한다. 패터닝 표면 카이랄 층은 특정 색을 띤 원형 편광 빛을 반사한다. 수평 배향 액정 층은 패터닝 표면 카이랄 층 위에 놓여져 반사된 빛의 편광 상태를 바꿀 수 있는 조정할 수 있는 위상 지연 소자의 역할을 한다. 액정 층에 가한 전압에 따라 오른손 원형 편광 혹은 왼손 원형 편광 이미지가

형성되고, 이는 편광판의 상태에 따라 저장된 이미지를 검출할 수 있다. 이 편광 변경 가능한 이미지 검출 시스템은 간단한 공정 과정, 높은 품질, 그리고 디스플레이와 이미지 저장 시스템을 포함한 시각적 응용분야에 다양하게 사용될 수 있다.

주요어: 이미지 선택, 카이랄 반응성 메소젠, 원형 편광, 액정

학번: 2016-20949